

## Numerical Investigation of the Passive Flow Control Around a Circular Cylinder

Tural TUNAY\*<sup>1</sup> ORCID 0000-0001-5994-4565

<sup>1</sup>Adana Alparslan Türkeş Science and Technology University, Faculty of Engineering  
Department of Mechanical Engineering, Adana, Türkiye

Geliş tarihi: 28.01.2023

Kabul tarihi: 28.03.2023

Atıf şekli/ How to cite: TUNAY, T., (2023). Numerical Investigation of the Passive Flow Control Around A Circular Cylinder. Cukurova University, Journal of the Faculty of Engineering, 38(1), 243-252.

### Abstract

The effects of a perforated cylinder on the passive flow control around a circular cylinder mounted on a wall were investigated. The perforated cylinder was placed outside of the single circular cylinder concentrically. The large-eddy simulation was used to resolve the flow field. The study was aimed at both reducing the drag coefficient of the single cylinder and controlling the fluctuating forces acting on the single cylinder caused by vortex shedding in the downstream wake. The results showed that the structure of the downstream wake flow of the single cylinder changed significantly after placing the perforated cylinder. For example, von Karman vortices disappeared, and the maximum magnitude of turbulent kinetic energy, TKE, in the downstream wake was reduced. The time-averaged drag coefficient of the single cylinder was decreased by 69%. In addition, the maximum value of the lift coefficient of the single cylinder was reduced by eight times when the perforated cylinder was placed outside the single cylinder.

**Keywords:** Cylinder, Drag, Flow control, LES, Vortex shedding

### Dairesel Silindir Çevresindeki Pasif Akış Kontrolünün Sayısal İncelenmesi

#### Öz

Mevcut çalışmada, delikli bir silindirin, duvara monte edilmiş dairesel bir silindir etrafındaki pasif akış kontrolü üzerindeki etkileri incelenmiştir. Delikli silindir, tek dairesel silindirin dışına eş merkezli olarak yerleştirilmiştir. Akış alanının çözümlenmesinde büyük girdap simülasyonu kullanıldı. Çalışma hem tekil silindir üzerine etkileyen sürüklenme kuvveti katsayısının azaltılmasını hem de aşağı akış bölgesinde girdap kopmalarından kaynaklanan ve silindir üzerine etkileyen değişken kuvvetlerin kontrol edilmesini amaçlamıştır. Sonuçlar, tekil silindirin aşağı akış girdap bölgesindeki akış yapılarının delikli silindirin eş merkezli olarak yerleştirilmesinden sonra önemli ölçüde değiştiğini ortaya koymuştur. Örnek olarak, von Karman girdap yapıları artık oluşmamıştır, ve aşağı akış girdap bölgesinde türbülans kinetik enerjisi

---

\*Corresponding author (Sorumlu yazar): Tural TUNAY, [ttunay@atu.edu.tr](mailto:ttunay@atu.edu.tr)

miktarı önemli ölçüde azalmıştır. Tek silindirin zaman ortalamalı sürtünme katsayısı değeri %69 oranında azalmıştır. Ayrıca, tek silindirin zamana bağlı kaldırma kuvveti katsayısının maksimum büyüklüğü, delikli silindir tek silindirin dışına eşmerkezli olarak yerleştirildikten sonra sekiz kat azalmıştır.

**Anahtar Kelimeler:** Silindir, Sürtünme direnci, Akış kontrolü, BGS, Girdap kopması

## 1. INTRODUCTION

Many industrial applications, which range from flow measurement to energy harvesting systems, involve flows around cylindrical objects. From an aerodynamics point of view, flows around cylindrical objects can be broadly classified as flows around bluff bodies which are characterised by separated flows, large recirculating flows in downstream wake and wake vortex shedding. The main problems generated by the flows around the cylindrical objects are the vibrations of cylinders owing to vortex shedding and significant drag coefficients due to pressure variations between the upstream and downstream regions of the cylinders. To lessen the negative consequences of the vortex shedding and the strength of the drag force, it is necessary to comprehend and regulate the flow characteristics surrounding cylinders.

In the previous literature, there are numerous studies in order to control the characteristics of the flows around cylinders [1-3]. Essentially, the control of flow around cylinders can employ either active or passive flow control techniques [4]. Both active and passive flow controls have their own advantages and disadvantages based on their applications. For example, a passive flow control does not need a power input whereas active flow control needs a power to actuate a moving attachment [5]. Furthermore, in active flow control the parameter which controls the flow can be varied according to the flow field as desired. On the other hand, passive flow control has a simplicity and a low cost [6]. There are many ways of applying passive flow control in the previous literature. For example, vortex generators [7], slats [8], flow vanes [9] and slits [10] are types of passive flow controls. The use of perforated structures is another type of the passive flow control in the previous literature [11]. The use of

perforated cylinders in the control of flow characteristics ranges from ocean engineering applications to heat transfer engineering [11,12].

The interaction of water waves with wall-mounted concentric cylindrical constructions, including a solid inner cylinder and a coaxial double-layered perforated cylinder, was studied by Liu et al. [13]. They concluded that there was a reduction in the hydrodynamic force operating on the inner cylinder as well as the wave height around its windward side. Additionally, Vijayalakshmi et al. [14] studied the wave acceleration and deceleration at the foremost and rearmost edges of the perforated cylinder that was concentrically placed outside of the single regular cylinder. They discovered that the incident wave height and the maximum wave inclination on the perforated cylinder were practically identical.

Sun et al. [15] defined two types of the flow mechanism in the downstream wake of the perforated cylinder with a regular cylinder placed concentrically inside it, depending on the porosity of the perforated cylinder, i.e.,  $\beta \leq 48\%$  and  $\beta \geq 61\%$ . They linked the first flow mechanism to the wake mode instability of the shear layers produced from the perforated cylinder's edge, and the second one with the merging of the shear layer vortices originating from the edge of the perforated cylinder with the vortices shed from the regular inner cylinder.

Durhasan et al. [16,17] experimentally investigated the characteristics of the flow around a cylinder with a perforated cylinder placed concentrically around it for various porosity and diameter ratios. Durhasan et al. [16] presented that the von Karman vortex street's formation was suppressed using perforated cylinders with porosity ratios between the ranges of  $0.4 \leq \beta \leq 0.8$ . In addition, they

discovered that the cylinder's drag coefficient was decreased by 21% to 87% in comparison to that of a single, conventional cylinder, depending on the porosity and diameter ratio [17]. Furthermore, Durhasan et al. [17] claimed that it is still unclear how the perforated cylinder affects the cylinder's lift coefficient.

The impacts of a perforated cylinder positioned concentrically outside of a single regular cylinder on the features of the wake flow that occurred downstream of the regular cylinder were examined numerically in the present study. The large eddy simulation (LES), resolving a wide range of time and length scales of a flow field, was used to resolve the turbulent flow field surrounding the cylinders. Thus, a high resolution of the flow field around the perforated and regular cylinders were presented using a high fidelity turbulence model, i.e., the LES, in the present study. Additionally, there are limited information about the pressure field occurring around the perforated cylinder used for the passive flow control of the wake downstream of the single regular cylinder. The present study showed the detailed results of the drag, lift and pressure coefficients, along with thorough explanations of the velocity field data.

## 2. MATERIAL AND METHODS

### 2.1. The Test Case

The geometric features of the single cylinder and the perforated cylinder, which are placed concentrically, are given in Figure 1. The diameters of the single cylinder and the perforated cylinder were  $D_i = 0.05$  m and  $D_o = 0.1$  m, respectively. The height of the cylinders was  $h = 0.35$  m. The radius of the holes on the perforated cylinder was  $R = 0.005$  m. The centers of the holes on the perforated cylinder were separated by a distance of  $0.0135$  mm. The porosity ratio of the perforated cylinder was  $\beta = 0.5$ . The porosity ratio,  $\beta$ , was calculated as the ratio of whole surface area of the holes on the cylinder to the total surface area of the cylinder.

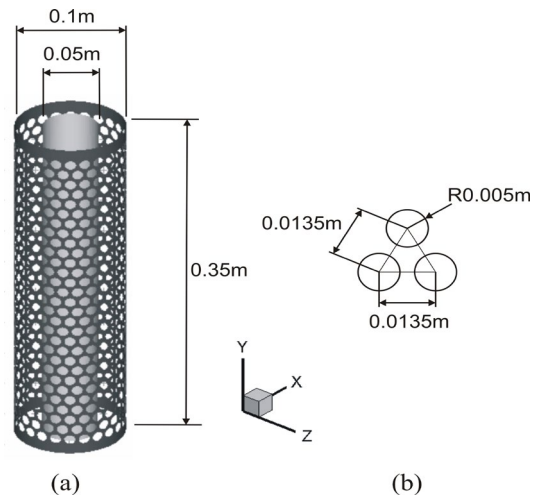


**Figure 1.** (a) The three-dimensional view of the wall-mounted, single regular cylinder and the perforated cylinder which are placed concentrically. (b) The geometric features of the holes on the perforated cylinder

### 2.2. The Features of the Flow Field

Figure 2 provides the computational flow domain's dimensions and boundary conditions. The cylinders were positioned  $11 \times D$  distance downstream from the flow domain's inlet surface. Also, the cylinders were placed at the symmetry location in the lateral direction. The height, length, and width of the flow domain were  $7 \times D$ ,  $52 \times D$ ,  $20 \times D$ , respectively. The Reynolds number, based on the diameter of the single regular cylinder,  $D_i = 0.05$  m, and the velocity of the free stream flow,  $U_\infty = 0.1$  m/s, was  $Re_D = 5000$ .

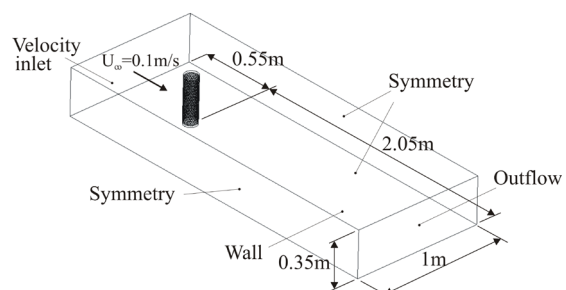


**Figure 2.** The computational flow domain's geometry and the boundary conditions

On the flow domain's inlet surface, a uniform velocity profile with a velocity of  $U_\infty = 0.1$  m/s was established. The turbulent intensity at the inlet surface was assumed to be zero. On the lateral and upper surfaces of the flow domain, symmetry boundary conditions were applied. A no-slip boundary condition was applied to the surfaces of the cylinders and the ground. Finally, on the exit surface of the flow domain, the outflow boundary condition was used.

In the investigations, the flows around a single cylinder with and without a perforated cylinder placed outside it were simulated in order to compare their results. Thus, two meshes were employed in the investigations. The mesh of the simulation of the regular cylinder without a perforated cylinder had 1608413 cells. On the other hand, the mesh of the simulation of the single cylinder with the perforated cylinder had 7160164 cells. General view of the computational mesh is given in Figure 3.

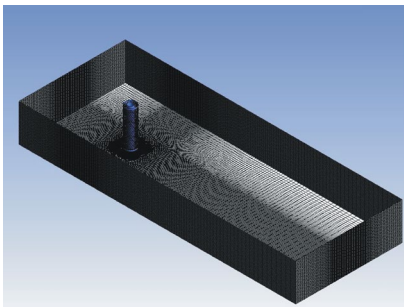


Figure 3. General view of the computational mesh

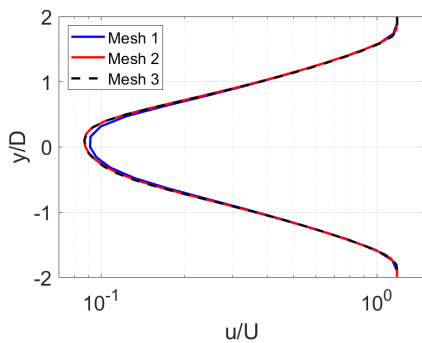


Figure 4. The velocity profiles which are obtained from different meshes at  $x/D = 6$  in the downstream wake region

Additionally, the results of the mesh independency study are presented in Figure 4 by comparing the profiles of the longitudinal velocity normalized with the freestream velocity at  $x/D = 6$ . The number of the computational cells in Mesh 1 to Mesh 3 were 4649874, 7160164, 8419225, respectively. The results obtained from Mesh 2 and Mesh 3 are close to each other. Therefore, Mesh 2 was decided to use in the computations.

The dimensionless wall distance,  $y^+$ , values on the cylinders' surfaces are presented in Figure 5. As shown in Figure 5, the  $y^+_{max}$  on the cylinders' surfaces are around 6.

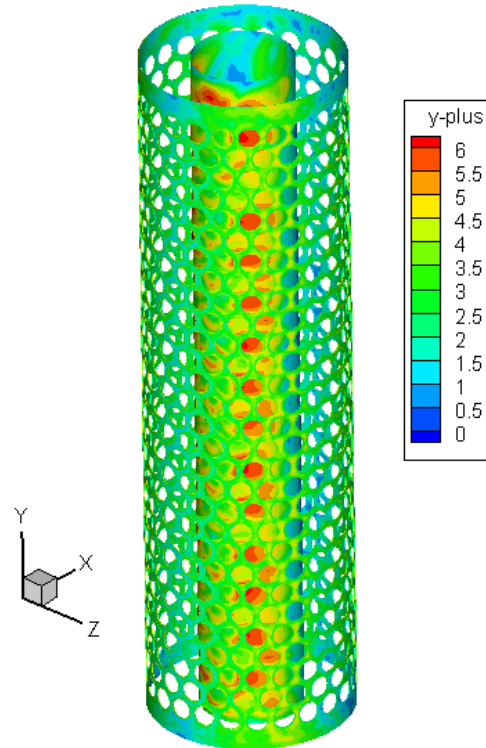
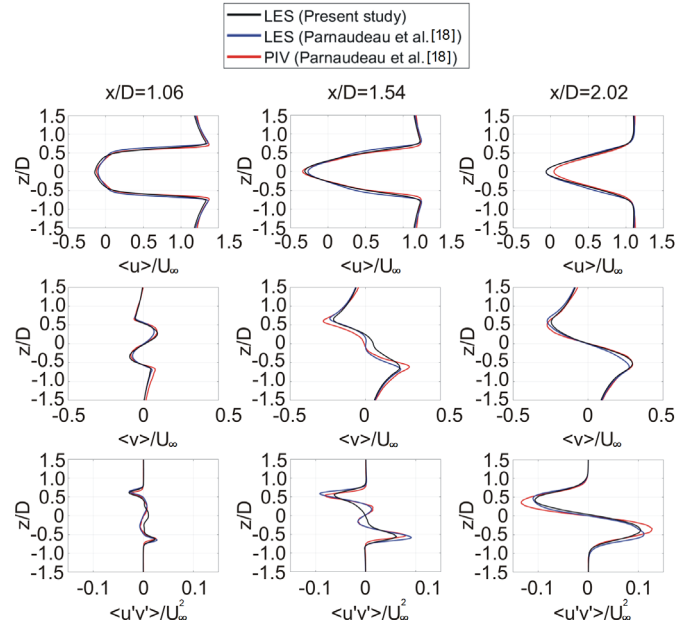


Figure 5. Contours of dimensionless wall distance,  $y^+$

Comparisons of the time-averaged x- and y-components of the velocities,  $\langle u \rangle / U_\infty$  and  $\langle v \rangle / U_\infty$  respectively, and time-averaged Reynolds stresses,  $\langle u'v' \rangle / U_\infty^2$ , obtained at three different locations in the downstream wake of the single cylinder with the corresponding experimental and numerical



**Figure 6.** Comparison of the time-averaged x- and y-components of the velocity results,  $\langle u \rangle / U_\infty$  and  $\langle v \rangle / U_\infty$  respectively, and time-averaged Reynolds stresses,  $\langle u'v' \rangle / U_\infty^2$  with the corresponding experimental and numerical results of Parnaudeau et al. [18]

results of Parnaudeau et al. [18] are given in Figure 6. In general, the results are coherent each other. The maximum differences between the  $\langle u \rangle / U_\infty$ ,  $\langle v \rangle / U_\infty$  and  $\langle u'v' \rangle / U_\infty^2$  results are less than 10%, 7%, 4% respectively. The maximum difference between  $\langle u \rangle / U_\infty$  results occurs on the vertical symmetry axis,  $z/D = 0$ , at  $x/D = 2.02$ . On the other hand, the maximum differences between the  $\langle v \rangle / U_\infty$  and  $\langle u'v' \rangle / U_\infty^2$  results occur on the shear layer after  $x/D = 1.54$ .

### 2.3. The Large Eddy Simulation

The large eddy simulation (LES) turbulence model was used to resolve the turbulent flow around the cylinders. The LES is a scale resolving high accuracy turbulence model that directly resolves large flow structures. The governing equations employed in the present study are given in Equations (1-5).

$$\frac{\partial \bar{u}_i}{\partial x_i} = 0 \quad (1)$$

$$\frac{\partial \bar{u}_i}{\partial t} + \frac{\partial}{\partial x_j} (\bar{u}_i \bar{u}_j) = -\frac{1}{\rho} \frac{\partial \bar{p}}{\partial x_i} + \nu \frac{\partial^2 \bar{u}_i}{\partial x_j \partial x_j} - \frac{\partial \tau_{ij}}{\partial x_j} \quad (2)$$

The subgrid-scale stress,  $\tau_{ij}$ , is defined by Equation (3).

$$\tau_{ij} = \rho \bar{u}_i \bar{u}_j - \rho \bar{u}_i \bar{u}_j \quad (3)$$

Equation (4) is a model for the subgrid-scale stress that results from the filtering procedure.

$$\tau_{ij} - \frac{1}{3} \tau_{kk} \delta_{ij} = -2\mu_\tau \bar{S}_{ij} \quad (4)$$

The  $\bar{S}_{ij}$  is defined by Equation (5).

$$\bar{S}_{ij} \equiv \frac{1}{2} \left( \frac{\partial \bar{u}_i}{\partial x_j} + \frac{\partial \bar{u}_j}{\partial x_i} \right) \quad (5)$$

### 2.4. Numerical Method

Governing equations of the flow were solved with the aid of commercial CFD software, i.e., Ansys Fluent. Pressure-based segregated algorithm together with SIMPLEC and PRESTO schemes

were used. The resultant scalar system of equations was solved by using a point implicit linear equation solver in conjunction with an Algebraic Multigrid method. The computations were performed with a time step of  $\Delta t = 0.002s$ . The simulation took 42s to complete.

### 3. RESULTS AND DISCUSSION

The goal of the current study was to examine the efficacy of using a perforated cylinder to manage the flow characteristics around a single, wall-mounted circular cylinder by positioning it concentrically outside of the cylinder. Therefore, the velocity and pressure fields which form around the cylinders were investigated using the streamlines, contours of velocity magnitudes, vorticity concentrations, turbulence quantities and force coefficients.

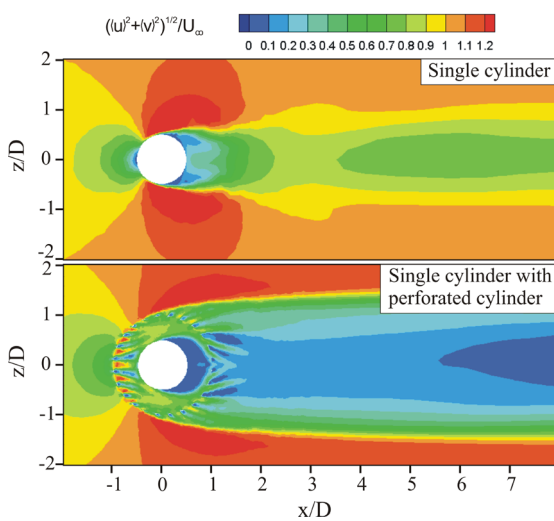


**Figure 7.** Contours of time-averaged velocity magnitude  $(\langle u^2 + \langle v^2 \rangle)^{1/2} / U_\infty$  in the  $xz$ -plane located at the vertical symmetry point of the cylinders,  $y = 0$

A comparison of the time-averaged velocity magnitude contours around a single cylinder and a single cylinder with a perforated cylinder is shown in Figure 7. An axial symmetry in the lateral direction, or  $z$ -direction, can be seen in the velocity magnitude contours surrounding the single cylinder. Besides, in the case of the single cylinder

with a perforated cylinder, the symmetry of the flow field around the cylinders is preserved. On the other hand, the structure of the flow field around the single cylinder changes significantly after the placement of the perforated cylinder outside of the single cylinder. For example, the stagnation region on the upstream part of the single cylinder disappears, and the size of the dead flow region enlarges in the wake region of the single cylinder. Additionally, the lateral size of the downstream wake of the single cylinder with the perforated cylinder increases proportionally to the diameter of the perforated cylinder. In line with the lateral size of the downstream wake, the size of the area that covers the minimum magnitude of the velocity contours extends towards the far region in the downstream wake of the single cylinder with the perforated cylinder.

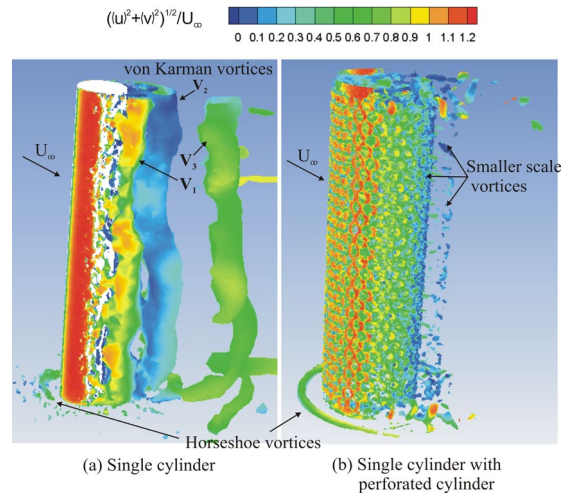


**Figure 8.** The instantaneous vorticity contours which are coloured by the velocity magnitude around the cylinders. Vortices are calculated by the Q-criterion

Figure 8 shows a three-dimensional view of the vortices formed around the cylinders. In this figure, Q-criterion is used for the calculation of the vortices. The vortices,  $V_i$ , developed in the downstream wake of the single cylinder present the characteristics of the large-scale von Karman vortices. These vortices form in the downstream

wake of the single cylinder periodically due to the flow separations on both the right and left lateral sides of the cylinder. After their development, these von Karman vortices shed in the wake flow and generate lifting forces that change their direction alternately. These large-scale von Karman vortices disappear in the case of the single cylinder with the perforated cylinder, and the small-scale vortices develop in the downstream wake. That means the perforated cylinder can help to reduce the unfavourable effects of the shedding forces caused by the vortices on the inner single cylinder.

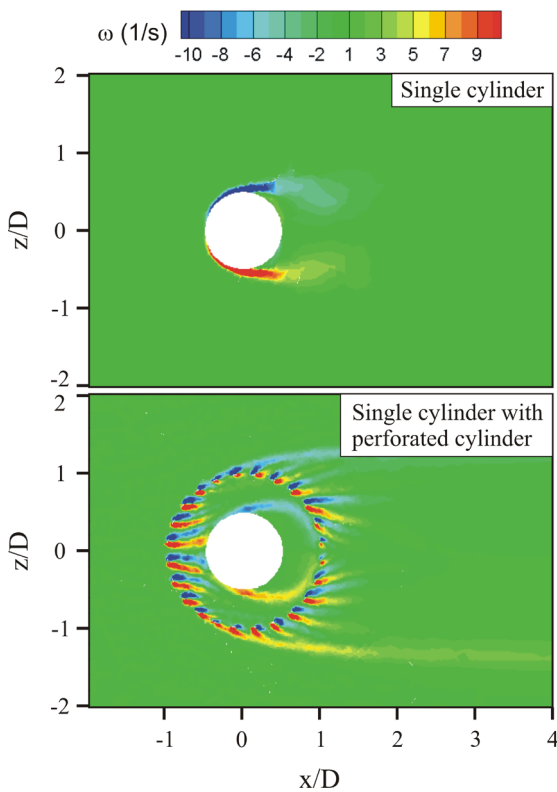


**Figure 9.** Time-averaged vorticity concentrations,  $\omega_y$ , in the  $xz$ -plane positioned at the vertical symmetry location of the cylinders,  $y = 0$

The time-averaged  $y$ -component of the vorticity concentrations,  $\omega_y$ , are presented in Figure 9. In line with the contours of the velocity magnitude

results, there is symmetry between the contours of the vorticity concentrations in the lateral direction, i.e.,  $z$ -direction, in both cases investigated. The counter-clockwise rotation of the vorticity concentrations is depicted by red contours, and the clockwise rotation is depicted by blue contours. The maximum magnitude of the vorticity concentrations developed around the single cylinder is decreased as a result of the perforated cylinder's placement outside of the single cylinder. Furthermore the length of the vorticity concentrations is constrained within the cross-sectional area of the perforated cylinder. Therefore, the shedding of the vortices in the downstream wake is prohibited by the perforated cylinder. Additionally, couples of the vorticity concentrations form downstream of each hole on the perforated cylinder.

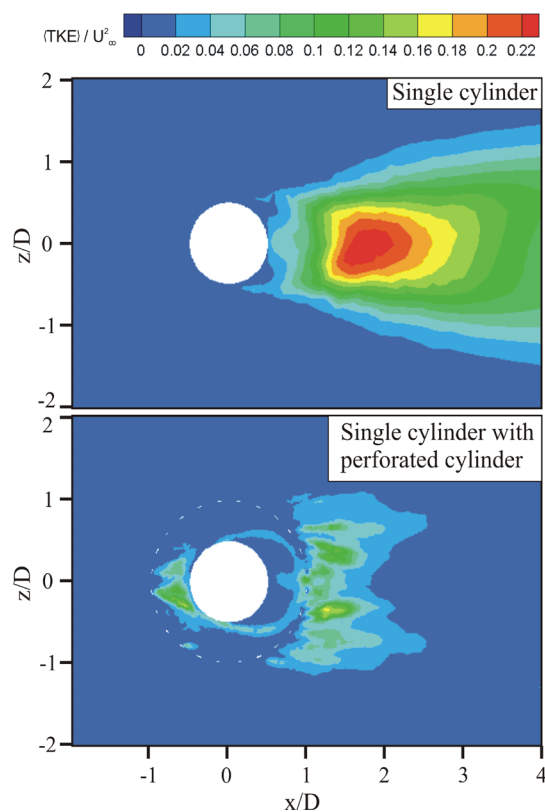


**Figure 10.** The time-averaged turbulent kinetic energy normalized by the square of the free stream velocity,  $\langle TKE \rangle / U_\infty^2$

Figure 10 displays the outcomes of time-averaged turbulent kinetic energy normalized by the square of the free stream velocity,  $\langle \text{TKE} \rangle / U_\infty^2$ . The results show that the maximum magnitude of the  $\langle \text{TKE} \rangle / U_\infty^2$  in the downstream wake of the single cylinder with the perforated cylinder is reduced considerably. Additionally, the perforated cylinder completely changes the distribution of the  $\langle \text{TKE} \rangle / U_\infty^2$  contours around the single cylinder. For example, a new region of increased  $\langle \text{TKE} \rangle / U_\infty^2$  appears in the upstream part of the single cylinder after placing the perforated cylinder outside of it.

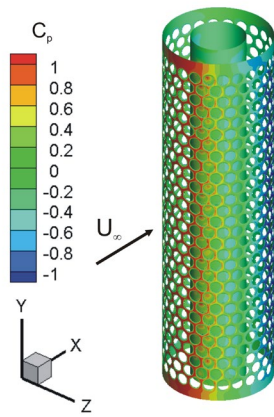


**Figure 11.** Time-averaged pressure coefficient results,  $\langle C_p \rangle$ , on the surfaces of the cylinders

Figure 11 shows that the maximum magnitude of the time-averaged pressure coefficient,  $\langle C_p \rangle$ , occurs at the stagnation point on the front surface of the perforated cylinder. Accordingly, the minimum magnitudes of  $\langle C_p \rangle$  occur on the rear surface of the perforated cylinder in the downstream direction. The magnitudes of  $\langle C_p \rangle$  on the surface of the regular cylinder are at moderate levels when compared to the ones that occurred on the surfaces of the perforated cylinder.

The time-averaged drag coefficients,  $\langle C_D \rangle$ , obtained from the single cylinder and the single cylinder with the perforated cylinder simulations are 1.09 and 0.34 respectively. The relative percent reduction in  $\langle C_D \rangle$  of the single cylinder after the perforated cylinder is placed outside of it is % 69.

Additionally, the unsteady lift coefficient,  $C_L$ , results obtained for both cases are presented in Figure 12. The lift coefficient results of the single cylinder show sinusoidal oscillations between the absolute maximum magnitudes of  $C_L = 0.4$ . These alternating oscillations in  $C_L$  of the single cylinder result are due to the alternating shedding of von Karman vortices developed in the downstream wake of the cylinder as presented in Figure 7, previously. On the other hand, the absolute maximum magnitude of the lift coefficient of the single cylinder is significantly reduced to a value of  $C_L = 0.05$ , i.e., eight times smaller than the one in the case of the single cylinder.

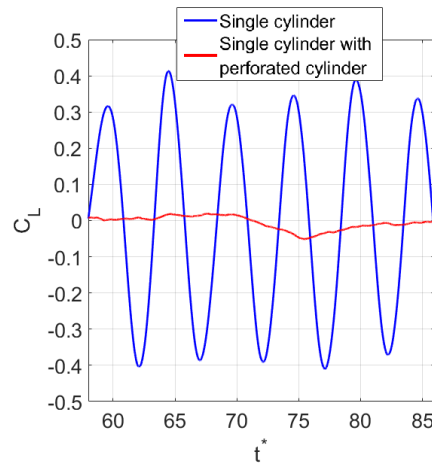


**Figure 12.** Comparison of the unsteady lift coefficient,  $C_L$ , results of the single cylinder and the single cylinder with the perforated cylinder simulations

#### 4. CONCLUSIONS

The goal of the current investigation was to determine how well a perforated cylinder could regulate the features of a wake flow that developed downstream of a single circular cylinder. The perforated cylinder was concentrically positioned outside of the single cylinder. The flow field was resolved using the large-eddy simulation method. The results showed that the structure of the downstream wake flow of the single cylinder changed significantly after placing the perforated cylinder outside of it, e.g., von Karman vortices

disappeared, and the maximum magnitude of turbulent kinetic energy, TKE, reduced. The time-averaged drag coefficient of the single cylinder was decreased by 69%. Additionally, the maximum magnitude of the lift coefficient of the single cylinder is decreased by eight times when the perforated cylinder was placed outside of the regular cylinder.

## 5. ACKNOWLEDGMENTS

The author acknowledges the support of the Mechanical Engineering Department, Adana Alparslan Turkes Science and Technology University, for providing computational support for this study.

## 6. REFERENCES

1. Ma, L.Q., Feng, L.H., 2019. Vortex Formation and Evolution for Flow Over a Circular Cylinder Excited by Symmetric Synthetic Jets, *Experimental Thermal and Fluid Science*, 104, 89–104. doi:10.1016/j.expthermflusci.2019.02.008.
2. Zhang, X., Choi, K.S., Huang, Y., Li, H.X., 2019. Flow Control Over a Circular Cylinder Using Virtual Moving Surface Boundary Layer Control, *Experiments In Fluids*, 60:104. doi:10.1007/s00348-019-2745-y.
3. Gao, D.L., Chen, G.B., Huang, Y.W., Chen, W.-L., Li, H., 2020. Flow Characteristics of a Fixed Circular Cylinder with an Upstream Splitter Plate: on the Plate-Length Sensitivity. *Experimental Thermal and Fluid Science*, 117, 110135.
4. Choi, H., Jeon, W.P., Kim, J., 2008. Control of Flow Over a Bluff Body, *Annu. Rev. Fluid Mech.*, 40, 113–39. doi:10.1146/annurev.fluid.39.050905.110149.
5. Tiainen, J., Grönman, A., Jaatinen-Värri, A., Backman, J., 2018. Flow Control Methods and Their Applicability in Low-Reynolds-Number Centrifugal Compressors - A Review, *Int. J. Turbomach. Propuls. Power*, 2018, 3, 2. doi:10.3390/ijtp3010002.
6. Paul, A.R., Joshi, S., Jindal, A., Maurya, S.P., Jain, A., 2013. Experimental Studies of Active and Passive Flow Control Techniques Applied in a Twin Air-Intake, *The Scientific World Journal*, 2013(523759), 8. doi:10.1155/2013/523759.
7. Ünal, U.O., Atlar, M., 2010. An Experimental Investigation into the Effect of Vortex Generators on the Near-Wake Flow of a Circular Cylinder, *Exp. Fluids* 48, 1059–1079. doi:10.1007/s00348-009-0791-6.
8. Chen, T., Jiang, X., Wang, H., Li, Q., Li, M., Wu, Z., 2021. Investigation of Leading-Edge Slat On Aerodynamic Performance of Wind Turbine Blade, *Proceedings of the Institution of Mechanical Engineers, Part C: Journal of Mechanical Engineering Science*, 235(8):1329-1343. doi:10.1177/0954406220941883.
9. Bari, S., Saad, I., 2013. CFD Modelling of the Effect of Guide Vane Swirl and Tumble Device to Generate Better In-Cylinder Air Flow in a CI Engine Fuelled by Biodiesel, *Computers & fluids*, 84, 262-269. doi:10.1016/j.compfluid.2013.06.011.
10. Gao, D.L., Chen, W.L., Li, H., Hu, H., 2017. Flow Around a Circular Cylinder with Slit, *Experimental Thermal and Fluid Science*, 82, 287–301. doi:10.1016/j.expthermflusci.2016.11.025.
11. Neelamani, S., Koether, G., Schuttrumpf, H., Muttray, M., Oumeraci, H., 2000. Wave Forces on, and Water-Surface Fluctuations Around a Vertical Cylinder Encircled by a Perforated Square Caisson, *Ocean Engineering*, 27, 775–800.
12. Acharya, S., Dash, S.K., 2018. Natural Convection Heat Transfer from Perforated Hollow Cylinder with Inline and Staggered Holes, *Journal of Heat Transfer*, 140, 032501-1. <https://doi.org/10.1115/1.4037875>.
13. Liu, J., Lin, G., Li, J., 2012. Short-Crested Waves Interaction with a Concentric Cylindrical Structure with Double-Layered Perforated Walls, *Ocean Engineering*, 40, 76–90.
14. Vijayalakshmia, K., Neelamanib, S., Sundaravadivelua, R., Murali, K., 2007. Wave Runup on a Concentric Twin Perforated Circular Cylinder, *Ocean Engineering*, 34, 327–336. doi:10.1016/j.oceaneng.2005.11.021.

15. Sun, C., Azmi, A.M., Zhu, H., Zhou, T., Cheng, L., 2021. Experimental Study on Wake Structures of a Circular Cylinder Enclosed in a Screen Shroud Using PIV, *Ocean Engineering*, 230, 109056. doi:10.1016/j.oceaneng.2021.109056.
16. Durhasan, T., Pinar, E., Ozkan, G.M., Aksoy, M.M., Akilli, H., Sahin, B., 2018. PIV Measurement Downstream of Perforated Cylinder in Deep Water, *European Journal of Mechanics/B Fluids*, 72, 225–234.
17. Durhasan, T., Pinar, E., Ozkan, G.M., Akilli, H., Sahin, B., 2019. The Effect of Shroud on Vortex Shedding Mechanism of Cylinder, *Applied Ocean Research*, 84, 51–61.
18. Parnaudeau, P., Carlier, J., Heitz, D., Lamballais, E., 2008. Experimental and Numerical Studies of the Flow Over a Circular Cylinder at Reynolds Number 3900, *Physics of Fluids*, 20(8), 085101.